Research Article

Designed synthesis of highly catalytic Ni–Pt nanoparticles for fuel cell applications

Kaneyuki Taniguchi[1] · Kozo Shinoda[2] · Jhon L. Cuya Huaman[1] · Shun Yokoyama[3] · Masahito Uchikoshi[2] · Takatoshi Matsumoto[2] · Kazumasa Suzuki[1] · Hiroshi Miyamura[1] · Balachandran Jeyadevan[1]

Abstract

A modified alcohol reduction process by controlling the complexation and reduction of metallic ions was developed to obtain compositionally and structurally controlled Ni–Pt nanoparticles (NPs) with sizes less than 20 nm in a high yield. The characterization of NPs synthesized under different experimental conditions suggested that the reduction of Pt and subsequent formation of cubic-shaped Ni–Pt NPs were strongly dependent on the formation of Pt-oleylamine (OAm) complexes. Thus, prior to the synthesis of Ni–Pt NPs, the formation and reduction process of Pt complexes in the solution-state were investigated by in situ UV–Visible and X-ray spectroscopies. The complexation of Pt ions along with their reduction prior to the formation of Pt metal and their influence on the size and the elemental distribution of Pt within the Ni–Pt NPs were revealed. Then, the above findings were actively utilized to design and to obtain Pt(core)–Ni(shell), Ni–Pt alloy, and Ni(core)–Pt(shell) nanostructures by regulating the OAm concentration in the system. The specific distribution of Pt on the Ni–Pt surface was confirmed by decolorization of methylene blue. Furthermore, Ni–Pt NPs with a Pt concentration of 10 at.% exhibited a mass activity four times larger than that of commercial Pt during the oxygen reduction reaction (ORR).

Keywords Ni–Pt nanoparticles · Complexation · In situ UV–Visible and X-ray spectroscopies · Fuel cell · Oxygen reduction reaction (ORR) · Catalysis

1 Introduction

Noble metal nanoparticles (NPs) with well-defined sizes, shapes, facets and compositions are being actively used in electronic, biological, medical, plasmonic and catalytic fields due to their exhibition of very specific properties compared to other metals [1–8]. Especially, platinum (Pt) is extensively used as it possesses high catalytic activity and stability. In the case of automobiles, Pt is used to convert the toxic exhaust gases such as carbon monoxide, NO_x and hydrocarbon into carbon dioxide, nitrogen and water. In another case, the use of Pt in fuel cells has been investigated extensively and the lethargic oxygen reduction reaction (ORR) on Pt is reported to limit their performance [9–13].

Furthermore, the size also has been found to affect the catalytic property of even in the nanoscale and NPs in the range of 30–1 nm has been observed to exhibit higher catalytic performance with decreasing size [14]. In addition to the size, the crystal plane is also considered to have an influence on the catalytic property. For example, in the case of dehydrogenating cyclization reaction of *n*-butane,

✉ Balachandran Jeyadevan, jeyadevan.b@mat.usp.ac.jp | [1]Department of Materials Science, The University of Shiga Prefecture, Hikone 522-8533, Japan. [2]Institute of Multidisciplinary Research for Advanced Materials, Tohoku University, Sendai 980-8577, Japan. [3]Graduate School of Environmental Studies, Tohoku University, Sendai 980-8579, Japan.

the reaction rate on Pt {111} has been found to be about five times that of {100} plane [15].

However, Pt is too expensive and their resource is limited. Thus, the reduction in consumption is being attempted by the following two techniques. One is to reduce the size of the catalyst particles, which subsequently leads to the increase in specific surface area. And the other is to alloy Pt with less costly elements (such as Co, Ni, Fe, etc.) that possess relatively moderate catalytic activities [16–30].

Alloying Pt with transition metals could lead to the modification of electronic structure of Pt, and the degree of its modification depends on the microstructure of the NPs with modified elemental distribution. The surface modification of NPs is reported to influence the electronic structure of Pt showing higher specific and mass activities for the ORR and methanol oxygen reduction (MOR) than the commercial Pt/C [31–34]. Similarly, the segregation of single Pt surface layer on Pt_3Ni (111) surface had permitted the discovery of phenomenally ORR active NPs which is considered due to shift in the electronic Pt valence d bands [35, 36]. Subsequently, concentrated effort on the synthesis and electrochemical investigation of octahedral skin Ni–Pt NPs has been promoted [37–39]. Furthermore, a delicate balance between the thickness of the Pt shells, the subsurface Ni content and the ratio of remaining {111} facets has been found to determine the ORR activity [40]. However, the Monte Carlo simulations have predicted that the formation of Pt skin 'surface-sandwich' structure could be realized irrespective of the shape and composition of particles [41].

Taking these findings into consideration, Ni–Pt NPs with different structures have been synthesized and high catalytic performances have been reported [34, 42–45]. However, in most cases, the NPs are synthesized mainly at elevated temperatures under prolonged reaction time, and also in small quantities. On the other hand, the authors succeeded in synthesizing novel Ni–Pt nanocubes with Pt segregated on their edges and corners at lower reaction temperatures by using 1-heptanol as a weak reducing agent [27]. The investigation on the growth mechanism of the Ni–Pt nanocubes revealed that the Pt atoms in the particle diffuse and reach the surface of the cubic-shaped Ni particles to form the Pt cage structure [46]. These particles exhibited about three times higher catalytic activity than the commercial Pt [21], due to its unique elemental distribution in nanoscale [46].

However, the drawback of this process was that the yield of the particles was very low due to the difficulty in reducing Pt ions. Consequently, the size was relatively large compared to conventional catalyst particles [46]. Considering the formation mechanism, the size and yield can be improved by increasing the number of Pt seeds

formed at the initial stages of the reaction. In the conventional method, oleylamine (OAm) influenced the formation of cubic shaped-Pt cage structure but large concentration of Pt ions remained in the solution even at the end the reaction. This is because OAm may have facilitated the formation of metal-OAm complexes [47], which are relatively difficult to reduce [46].

All the above studies suggest that the potential of Pt or Pt-based catalysts is immense and the development of morphologically and structurally controlled Pt nanostructures or novel Pt-based materials is urgently required to meet the ever-increasing demand in the energy and related fields. However, it should be noted that the synthesis of Pt or Pt-based alloy catalyst NPs is only the consequence of the synthesis process employed. Though limited information related to the formation process is revealed in some cases, the designed-synthesis of Pt-based alloys has not been achieved due to lack of information during the synthesis, especially at ionic states in liquid prior to the formation of the solid precipitation.

Therefore, the formation of Pt seeds in the initial stages of the reaction and the growth mechanism of these NPs needs to be studied to design Pt-based alloys. In this work, a novel reaction cell has been designed by the authors to carry out in situ UV–Vis and in situ XAS measurements for the evaluation of the structural changes of Pt precursor during the reaction in the liquid. The details of the reaction cell is given in the experimental section.

Thus, a novel synthesis technique is developed in the present study to obtain a large number of Pt seeds that subsequently get coated with nickel. This result in obtaining small-sized core (Pt)–shell (Ni) NPs in high yield, in which the Pt atoms diffuse to the surface as the reaction progresses [46]. The catalytic property evaluated using decolorization reaction of methylene blue confirmed the successful synthesis of designed Ni–Pt NPs with varying Pt distribution on the surface. Furthermore, electrocatalytic properties of Ni–Pt NPs and commercial Pt NPs were attempted through the ORR in acidic system.

2 Experimental section

2.1 Materials

Nickel(II) acetate tetrahydrate ($Ni(OAc)_2 \cdot 4H_2O$, 98% purity), and dihydrogen hexachloroplatinate hexahydrate ($H_2PtCl_6 \cdot 6H_2O$, 98.5%), sodium borohydride ($NaBH_4$, 90.0%), methylene blue and solvents such as 1-heptanol (98%), methanol (99.8%), toluene (99.5%), nitric acid (69%), hydrochloric acid (36%) were purchased from Wako Pure Chemicals Ltd., Japan. Oleylamine (OAm, 70%) were purchased from Sigma-Aldrich Co.

2.2 Synthesis of Ni–Pt NPs

In a typical procedure to synthesize Ni–Pt NPs, 100 mL 1-heptanol containing 0.2 mmol $H_2PtCl_6\cdot6H_2O$ and OAm was heated from room temperature (R.T.) to 130 °C at a heating rate of 10 °C/min. Once the color of the solution just changed from yellow to black in around 60 min at 130 °C, a solution containing 3.8 mmol of $Ni(OAc)_2\cdot4H_2O$ and 42 mmol of OAm was injected. Then, the temperature of this mixed solution was raised from 130 to 173 °C and kept at this temperature for 2 h. The resulting NPs were collected using a magnet and washed with a mixture of methanol and toluene to remove unreacted compounds and excess OAm. The NPs were finally re-dispersed in toluene.

2.3 Theoretical estimation of (Pt, Ni)-OAm binding energy

Three-dimensional coordinates of target molecules were obtained by using CS Chem 3D Ver. 7.0 [48]. The coordinates of the prepared target molecule were sufficiently optimized by using HF/Lanl2DZ in Gaussian 09 Rev. E.01 [49]. Lanl/2DZ [50–53], which is one of the effective core potentials, is used for including metal atoms. Regarding the adsorption energy between alkylamine and metal, conformational isomers of the target molecule were neglected in order to avoid complexity derived from conformers. Also, in order to minimize the interactions to be considered, the alkyl chain moiety in the target molecule was assumed linear. Regarding the evaluation of adsorption energies, single point calculations were performed at distances between the optimized target molecule and the metal from 1.50 to 20.0 Å. The reference point of energy was assumed at 20.0 Å since the first derivative of energy at this point was almost 0. From this, the adsorption energy was defined as the energy difference between the energy at reference point to the point at which the energy was most stable.

2.4 In situ measurements of structural changes of Pt precursor during the synthesis

In situ X-ray absorption spectroscopy (XAS) measurements were carried out at Engineering Science Research II Beamline (BL14B2) at SPring-8, Japan using a reaction cell designed by the authors to perform XAS and UV–Vis measurements of the reactants simultaneously from R.T. to 173 °C. The reaction cell was made of aluminium with quartz glass window at the lower section of the cell for UV–Vis measurements and a Kapton window at the upper section for XAS measurements. The schematic diagram of the cell and the photograph of the experimental

setup are given in Fig. 1. The reactants used for the measurements are as follow: 0.01 mmol of $H_2PtCl_6\cdot6H_2O$, and 40 mmol of OAm were dissolved in 25 mL of 1-heptanol. Then, 5 mL of the above solution was introduced into the reaction cell and heated from R.T. to 130 °C at a heating rate of 6 °C/min and maintained at this temperature for 3 h. The XAS measurements were made at Pt-L edges using 19 element SSD in the fluorescence mode. In situ UV–Vis was carried out in the wavelength range of 200–800 nm by using deuterium (200–400 nm) and halogen (400–800 nm) lamps. UV–Vis and XAS measurements were carried out continuously during heating till the particles are formed. For identification of complexes formed in the liquid state of the reaction, FEFF (version 8.2) was used. It is a program designed to fit experimental XAFS spectra using predetermined model clusters of atoms from FEFF.

2.5 Characterization

The powder X-ray diffraction patterns of the vacuum dried samples were measured using an X-ray diffractometer (XRD; Rigaku Smart Lab 3) with Cu-Kα radiation to identify the crystal phases present. The size and morphology of the particles were assessed using the transmission electron microscope (TEM; Hitachi H8100) operated at 200 kV. The samples for TEM measurement were prepared by depositing a toluene dispersion of Ni–Pt particles on amorphous carbon-coated grids. In addition, high-angle annular dark field (HAADF) microscopy, coupled with scanning transmission electron microscopy (STEM) and energy-dispersive spectroscopy (EDS) elemental mapping, were performed on a JEOL JEM-ARM200F instrument operated at 200 kV with a spherical aberration corrector; the nominal resolution was 0.8 Å. STEM-HAADF imaging and EDS mapping analysis allowed us to clearly visualize the relative positions of Ni and Pt within the individual Ni–Pt NPs.
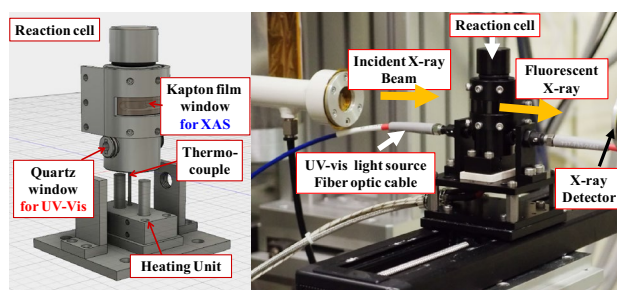

Fig. 1 Schematic diagram of the cell for in situ XAS and UV–Vis measurements (left side) and the photograph of the experimental setup (right side) used during the measurement at SPring-8 Beamline BL14B2

2.6 Chemical composition of the NPs

The chemical composition of Ni–Pt NPs sampled under different synthesis conditions were analysed using inductively-coupled plasma mass spectrometer (ICP-MS; SII SPS3100). The samples were prepared by dissolving the Ni–Pt NPs in aqua regia and the Ni and Pt contents were evaluated from the calibration curves obtained using the standard solutions of Pt and Ni.

2.7 Catalytic properties of Ni–Pt NPs in the decolouration reaction of methylene blue

In a typical method [54], 5 mL $NaBH_4$ solution (20 mmol) and 22.5 mL methylene blue solution (9×10^{-2} mmol) were mixed in a glass beaker. In another beaker, 1 mg of Ni–Pt NPs were dispersed in 12.5 mL distilled water. Both solutions were mixed and then 4 mL of the solution was withdrawn every minute for UV–Vis absorbance measurement (Hitachi U-3900) in the range between 500 and 800 nm. The methylene blue solution absorbs part of the visible light and exhibits maximum absorbance at 664.5 nm.

2.8 Electrocatalytic properties of Ni–Pt NPs

The samples for electrocatalytic measurements were prepared as follows: 80 mg of ketjen black EC 600 powder that was heated at 850 °C for 5 h under an Ar gas flow of 100 mL/min was dispersed in 100 ml of toluene. The suspension was ultrasonicated for 30 min to disperse the ketjen black well prior to the addition of 20 mg of Ni–Pt NPs. Then, the suspension was stirred at 500 rpm for 2 h to obtain Ni–Pt deposited ketjen black (Ni–Pt/C). Finally, the Ni–Pt/C was recovered from the suspension using a vacuum filter and subsequently heated under a constant Ar/H_2 (3% H_2) flow of 100 mL/min at 400 °C for 2 h to remove the surfactant. Then, isopropanol, Nafion and Ni–Pt/C powder were mixed and subsequently dried to form the electrodes. Cyclic voltammetry (CV) was carried out using the electrode prepared. The CV measurement was carried out at 25 °C using N_2 gas saturated 0.1 M $HClO_4$ as the electrolyte under a sweeping range and speed of 0.05–1.00 V and 50 mV s^{-1}, respectively. The electrochemically active surface area (ECSA) was evaluated from the hydrogen absorption curve. Linear sweep voltammetry (LSV) curve was obtained by rotating the disk at 400, 900, 1600 and 2500 rpm measuring mass activity through the ORR under a sweeping range and speed of 0.20–1.20 V and 10 mV s^{-1}.

3 Results and discussion

3.1 Effect of oleylamine on the synthesis of Ni–Pt NPs

In the synthesis of Ni–Pt NPs with Pt cage structure, the concentration of OAm influenced the size, cubic-shape and segregation of Pt on the edges and corners of the cube [29]. This was believed due to the formation of metal-OAm complexes that deters the reduction of Ni and Pt ions. Thus, to enhance the reaction efficiency, initially the synthesis of Ni–Pt was carried out for prolonged period of time following the experimental conditions reported by Nagao et al. [46]. Though the reaction time was extended from 2 h to 4 h, a marginal increase of the yield from 50.2 to 56% was observed. Furthermore, the chemical composition was determined to be $Ni_{95}Pt_5$ indicating a low reduction of Pt ions compared to Ni in spite the initial molar ratio between Ni and Pt was 80:20. To understand the reason, the synthesis of Ni was attempted at 173 °C using $Ni(OAc)_2 \cdot 4H_2O$- 1-heptanol (Ni-Hep) and $Ni(OAc)_2 \cdot 4H_2O$-1-heptanol-OAm (Ni-Hep-OAm) systems. Surprisingly, in both cases, the reduction of Ni ions was completed within 1 h. Furthermore, the reduction of Pt at 130 °C using $H_2PtCl_6 \cdot 6H_2O$- 1-heptanol (Pt-Hep) system was also completed within 1 h. In contrast, the reduction of Pt ions was not possible at 130 °C in $H_2PtCl_6 \cdot 6H_2O$-1-heptanol- OAm (Pt-Hep-OAm) system, and required high temperature and longer reaction time. The above results envisaged the formation of a complex between Pt and OAm. Although oleylamine has been considered to influence in metallic reduction, [47] the formation of metal-OAm complexes, their stability and reducibility are not well-known.

Thus, to estimate the relative stabilities between Pt- and Ni-OAm complexes, the binding energies were calculated using molecular orbital theory. The relative binding energies were derived from the difference between binding energies at 20 Å and at other distances. The relative binding energies for Pt and Ni with OAm were evaluated to be
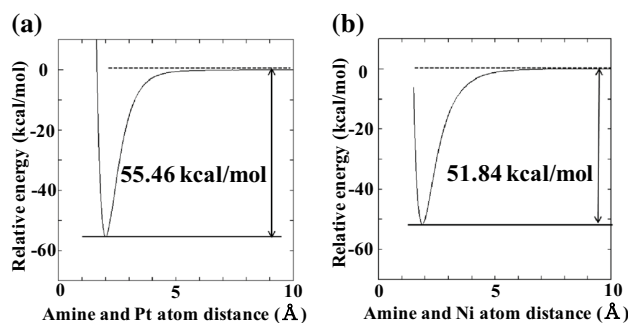

Fig. 2 Adsorption energy between amine and **a** Pt and **b** Ni atoms

55.64 and 51.84 kcal/mol, respectively as shown in Fig. 2. The results suggested that OAm binds strongly with Pt than Ni. Therefore, the preferential bonding of OAm with Pt to form Pt-OAm complex could have inhibited the reduction of Pt ions. However, experimental information related to the complexation of metals with OAm and their stability in the solution state has not been verified in the past. To investigate the formation of metal complex in the solution, prior to the reduction of the metal ions, the in situ UV–Vis and XAS measurements of the solutions in the temperature range between R.T. and 130 °C were performed using the reaction cell shown in Fig. 1.

3.2 Elucidation of formation mechanism of Pt complexes and their reduction using in situ UV–Vis and XAS

To understand the behavior of Pt ions in different systems, first, in situ UV–Vis measurements were performed on Pt-Hep, $H_2PtCl_6 \cdot 6H_2O$-OAm (Pt-OAm), and Pt-Hep-OAm (Hep/OAm = 30) solutions from 0 to 60 min at 130 °C and Pt-Hep-OAm solutions with different molar ratios of Hep/OAm at 130 °C for 0 min. The results are shown in the supporting information (Fig. S1). Since the absorption spectra obtained in the cases of Pt-Hep (Fig. S1(a)) and Pt-OAm (Fig. S1(b)) differed, the Pt complexes formed in the above cases are inferred to be different. And interestingly results were obtained in the case of Pt-Hep-OAm, these exhibited temperature dependent profiles. At the beginning, the absorption spectrum was very similar to the profile corresponding to Pt-Hep.

However, when the solution was heated to higher temperatures, the absorption spectra became very similar to that of Pt-OAm and the peak red-shifted from 290 to 300 nm (Fig. S1(c)). Furthermore, when the absorption spectra under varying OAm concentrations were compared, the peak red-shifted considerably with increasing OAm concentrations (Fig. S1(d)). Based on the above results, the following mechanism can be proposed. At the initial stages of the reaction, the Pt^{4+} ions coordinated with the hydroxy group (–OH) from 1-heptanol and as time progressed these were replaced with amino group (–NH_2). Furthermore, as coordination with amino group progressed, the reduction became difficult. However, the reduction mechanism of Pt was still not clear. To acquire additional information, investigations on the structural changes that could have taken place during heating were performed using in situ XAS studies.

For the XAS studies, Pt-Hep and Pt-Hep-OAm solutions were considered. The above solutions were heated at specific temperatures for different durations. Figure 3 shows the behavior of Pt precursor in 1-heptanol measured by XAS and UV–Vis spectroscopy at different temperatures during heating and at 130 °C from 0 to 60 min measured using Engineering Science Research II beamline (BL14B2) at SPring-8. As the reaction temperature is raised, the intensities of the post-edge peak in the Pt L3 X-ray Absorption Near Edge Structure (XANES) profiles decreased as shown in Fig. 3a. The post-edge peak depends on the valence of Pt ion and the decrease in the intensity suggests the reduction of Pt^{4+} ions to Pt^{2+} ions. Furthermore, the XANES profile at 130 °C after an elapsed time of 26 min

Fig. 3 XANES spectra at Pt L3-edge measured at 130 °C for different reaction times in **a** Pt-Hep and, **b** Pt-Hep-OAm systems. UV–Vis spectra measurements of Pt-Hep system **c** during heating, **d** from 0 to 60 min at 130 °C and **e** Pt-Hep-OAm solution at 130 °C for different reaction times
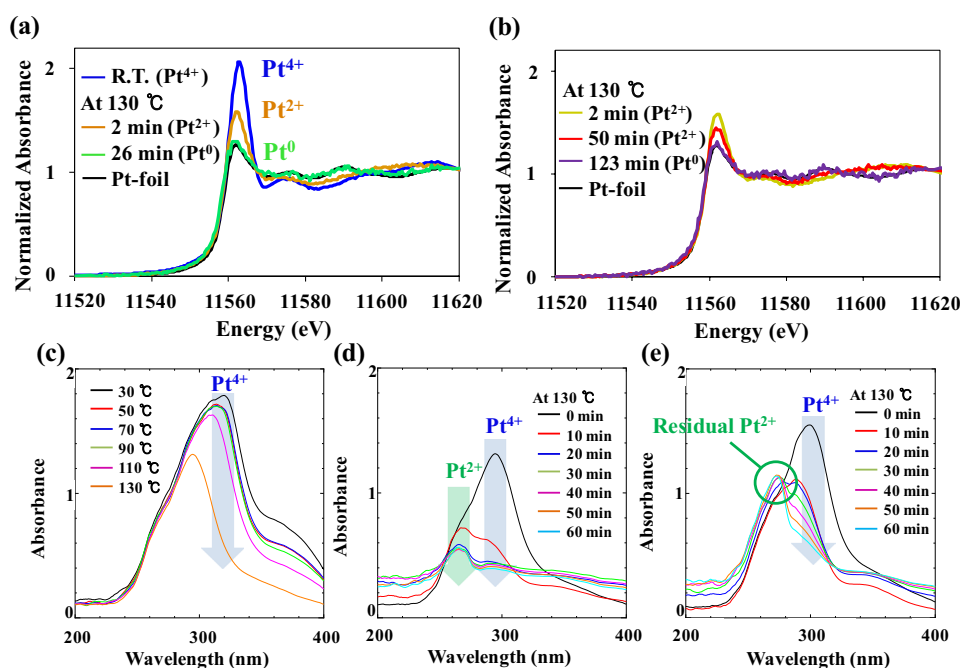
exactly matched with that of Pt-metal reference suggesting the formation of metal Pt particles.

Furthermore, variation in the absorption profile was also observed in the UV–Vis spectra obtained simultaneously (Fig. 3(c)). At room temperature, absorption peaks at around 265, 300 and 320 nm were observed. It should be noted that the variation in the UV–Vis absorption spectra (intensity and shift) at around 300 and 320 nm was observed almost at the same time when the XANES spectra exhibited a change from the initial state with the increase in the reaction temperature. The peak around 265 nm is assumed to correspond to Pt^{2+}. It has been reported that the absorption peaks corresponding to Pt^{4+} and Pt^{2+} in ethylene glycol were 212 and 268 nm, and 212 and 228 nm, respectively [55]. From the above results, it could be inferred that the peak corresponding to Pt^{4+} appears at higher wavelength compared to Pt^{2+} and thus Pt^0 is obtained via the reduction of Pt^{4+} to Pt^{2+} [56, 57]. At 130 °C, the intensity of the UV–Vis peak corresponding to Pt^{4+} decreased and the baseline of the spectra increased as shown in Fig. 3d. This behaviour indicates the formation of metallic Pt NPs. The shape of the XANES spectra under similar conditions proved the same.

Figure 3b shows the XANES spectra at Pt L3-edge of Pt-Hep-OAm (OAm/Pt ratio = 1) solutions. Though the reduction of Pt^{4+} to Pt^{2+} occurred around the same duration, the conversion of Pt^{2+} to Pt^0 was delayed in comparison with Pt-Hep case as shown Fig. 3a. On the other hand, a considerable variation in the UV–Vis absorption spectra occurred after an elapsed time of 50 min at 130 °C as shown in Fig. 3e. The above results suggested that the OAm coordinated with Pt to form Pt-NH_2 complex and facilitated the reduction of Pt^{4+} to Pt^{2+} relatively easily; however, the reduction of Pt^{2+} to Pt^0 was deterred. In fact, the degree of reduction was low when the OAm concentration was increased as shown in Fig. 5a.

The Pt L3 Extended X-ray Absorption Fine Structure (EXAFS) spectra Fourier transformed and inverse Fourier transformed profiles of Pt-Hep solution at R.T. and at 120 °C, Pt-Hep-OAm solution for OAm/Pt ratios of 1 and 200 at 130 °C and Pt-OAm solution 130 °C are shown in Fig. 4a, b.

From the results, Pt ions present in the solution at either 120 °C or 130 °C are in the divalent state. Next, the radial structure function of each EXAFS spectrum was obtained by Fourier transformation. And then, the structure of the Pt complex was determined by the fitting the EXAFS wave function obtained from inverse Fourier transformed peak corresponding to the first nearest neighbour (Fig. S2). There was no considerable difference between the EXAFS spectra of Pt-Hep and Pt-Hep-OAm (OAm/Pt = 1). Here, the Pt ions are in the tetravalent state (Pt^{4+}) and are given in Fig. S2(a), (b). Fig S2(d), (e) refers to cases where Pt ions

are in the Pt^{2+} state. In the case of Pt^{4+}, Pt is coordinated with neither O nor N, both in the absence and in the low concentration of OAm. It is believed that Pt is coordinated with Cl^- ions from $H_2PtCl_6 \cdot 6H_2O$ [58]. In the case of Pt^{2+} (Fig. S2(d), (e)), it is required to distinguish the coordination of -OH with that of -NH_2. However, the distinction between O and N is considered difficult since O and N are neighbouring atoms and the back-scattering amplitude and phase shift are almost similar. However, -NH_2 could partially coordinated even at low concentration of OAm because, when the OAm/Pt ratio increased to 200, there was a considerable difference in the EXAFS spectra (Fig S2(f)), which indicates that –NH_2 have been coordinated for certain.

EXAFS analysis suggested that Pt^{4+} coordinated with Cl^- derived from the precursor salt either in the absence or in the presence of low concentration of OAm. However, when Pt^{4+} is reduced to Pt^{2+}, it coordinates with either –OH or –NH_2 derived from 1-heptanol or OAm, respectively. Furthermore, it should be noted that at higher OAm concentrations, the coordination of –NH_2 with Pt^{4+} and Pt^{2+} is confirmed. These results suggested that the binding of –NH_2 is comparatively higher than that of –OH and Cl^-. A proposed scheme describing the structural changes of Pt precursor during heating is shown in Fig. 4c.

3.3 Development of a synthesis scheme for high yield Ni–Pt NPs

It is very clear from the in situ analyses that the easiness with which the Pt nucleus is formed depends on the OAm concentration (Fig. 5a). Thus, an attempt to control the formation of Pt nucleus was performed by changing the concentration of OAm, not only to increase the yield but also to improve the quality of Ni–Pt NPs. First, Pt particles were synthesized without OAm. After that, the solution containing Ni salt and OAm was injected into the solution containing Pt particles. Here, a high yield of Ni–Pt NPs was expected through the formation of a large number of Pt seeds that get subsequently coated with Ni. In addition, as the reaction time progressed, diffusion of Pt from the Pt seeds to the particle surface to form Pt cage structured Ni–Pt NPs was expected [46]. The yield of Ni and Pt was estimated by introducing $NaBH_4$ into the spent solution to evaluate the concentration of unreacted metal salts. However, no particles were detected suggesting that the yield of Ni–Pt NPs is almost 100%. As shown in Fig. 5c, the average size of Ni–Pt NPs was 24.9 nm whereas the elemental mapping results revealed the presence of Pt core and no diffusion of Pt to the particle surface was detected. Furthermore, separate phases of Pt and Ni were also detected in the XRD profile (Fig. 5b). The reason for the above behavior was due to the large gap between the

Fig. 4 **a** Fourier transformed and **b** inverse Fourier transformed profiles of Pt L3 EXAFS spectra measured under different temperature and OAm concentration. **c** Scheme describing the structural changes of Pt^{4+} ions during reduction reaction in absence and presence of OAm
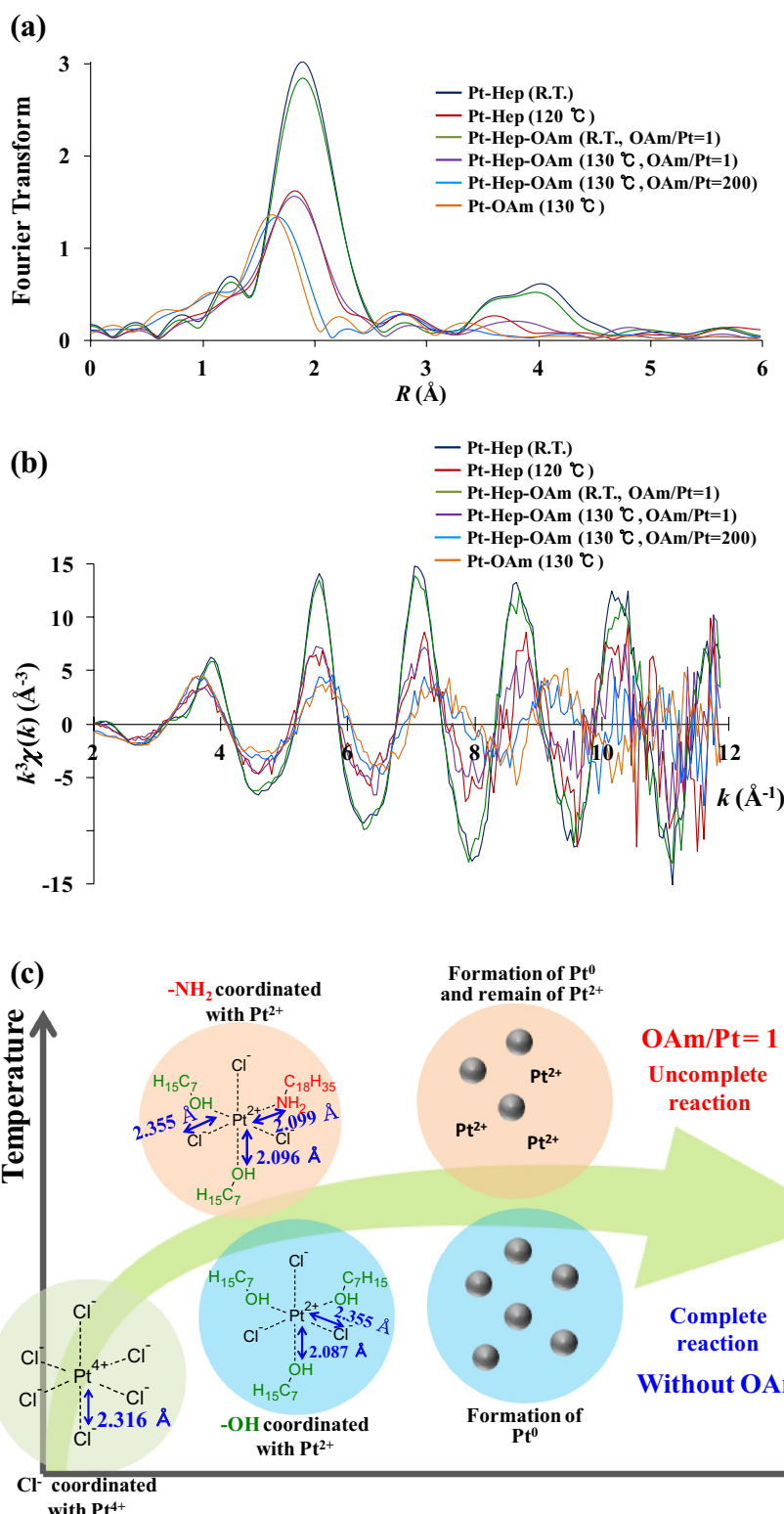
time at which Pt and Ni were reduced. Generally, Pt atoms (0.139 nm), whose atomic radius is much larger than that of Ni atoms (0.124 nm), tend to migrate outwards to relieve the internal strain during the formation of an alloy [59].

This tendency could be much stronger at higher Ni concentration. However, in this case, when Ni ions began to get reduced, no Pt ions existed in the solution. Thus, the formation of alloy NPs was not facilitated. Consequently,

Fig. 5 **a** The influence of OAm concentration on the yield of Pt NPs, **b** XRD patterns, **c–f** TEM images and elemental mapping of Ni–Pt NPs synthesized under different OAm/Pt and Ni/Pt ratios
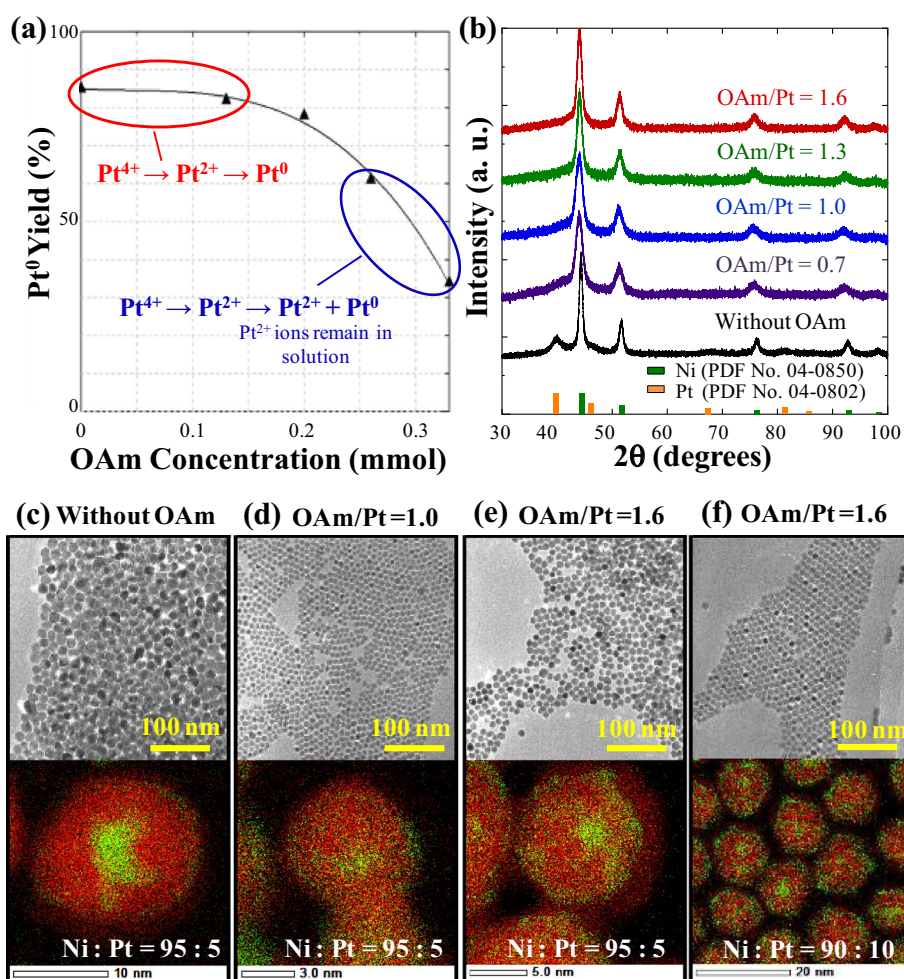
Pt core was formed and no diffusion of Pt was observed. Since the catalytic reaction occurs on the surface of the catalyst, these NPs are predicted to be unsuitable as a catalyst.

TEM and elemental mapping images of the Ni–Pt NPs synthesized by controlling the concentration of OAm during Pt nucleation are shown in Fig. 5d, e for OAm/Pt molar ratios of 1.0 and 1.6, respectively. The size of Ni–Pt decreased compared to OAm-free case and the size decreased with increasing OAm/Pt molar ratio. The average size decreased from about 25 to 14 nm. Though the number nucleus formed in the OAm-free case is expected to be high due to the high reduction rate [60], the subsequent aggregation of the nucleus is believed to have caused the increase in particle size. The yields of Ni–Pt NPs synthesized under both cases were determined to be 100%. This was confirmed by chemical analysis of the spent solution. Though the presence of Pt was observed at the centre of the particle in the OAm-free case, their appearance on the particle surface was apparent only for low OAm concentrations (Fig. 5d, e). Similar behaviour was

observed when the samples synthesized with a Ni:Pt precursor ratio of 95:5 was changed to 90:10 (Fig. 5f). This is believed due to the inhibition of the reduction of Pt ions at low temperature, promotion of co-reduction of Pt and Ni and subsequent diffusion of Pt ions to the surface. The above speculation was also confirmed by XRD analyses (Fig. 5b). Though the diffraction lines corresponding to Pt and Ni appeared separately in OAm-free case, the peaks corresponding to Ni phase shifted towards lower angle from 44.3 to 44.1 degrees, and the peaks corresponding to Pt (111) merged with that of Ni (111) suggesting the progression of alloy formation. The detailed elemental distribution of Ni and Pt for the particles synthesized under different OAm/Pt ratio is given in supporting information (Fig. S3).

The reduction in the size of the above particles with the increase in OAm concentration is believed due to the surface protective effect that inhibited the aggregation of particles. Furthermore, the yield was not influenced by the addition of a small amount of OAm and the composition of the particles was almost similar to the initial ratio between

Pt and Ni. The details on the influence of the OAm concentration in the composition, size, and structure of synthesized Ni–Pt NPs are shown in Table 1. When the particle sizes and crystallite sizes are compared, the particle size is larger than the crystallite size in all cases. This suggests that the particles synthesized here are polycrystalline. It should be noted that the crystallite size is larger for high OAm concentration. This could be due to retardation of the reaction rate through complexation of Pt with OAm.

The formation mechanism of the synthesis scheme proposed for Ni–Pt particles under different concentrations of OAm is shown in Fig. 6. By controlling the complexation between Pt^{4+} and OAm, not only the yield but also the segregation of the nucleus and subsequent growth was inhibited. Consequently, the delay in the reduction of Pt-complex facilitated the alloying of Pt with Ni and successful synthesis of Ni–Pt particles with varying degree of Pt segregation on the surface of the particle is realized.

Fig. 6 Scheme showing the influence of OAm in the formation of Pt-OAm complexes and their reduction to obtain Pt(core)–Ni(shell) and Ni(core)–Pt(shell) NPs

3.4 Catalytic activity of Ni–Pt NPs with varying sizes and compositions

The high catalytic activity of bimetallic NPs has been ascribed to several factors such as the high surface area, shape, and the surface composition [61]. In this study, the designed-synthesis of Ni–Pt NPs with controlled segregation of Pt on the surface has been achieved. Thus, the catalytic activity of the synthesized Ni–Pt NPs with different surface distribution of Pt are evaluated using the decolouration of methylene blue by using $NaBH_4$ (Fig. S4). Here also, Ni and Pt NPs were used as reference as shown in Fig. S4 (a) and (b), respectively. In the case of Ni NPs, the decolorization reaction was not observed whereas the reaction was very rapid in the case of Pt NPs. Using Pt NPs, the peak corresponding to methylene blue disappeared and the decomposition reaction ended within 4 min. Taking these results into account, the core–shell structured Pt-Ni NPs did not decompose the methylene blue (Fig. S4 (c)) due to the absence of Pt on the particle surface as already confirmed through the elemental mapping (Fig. 5).
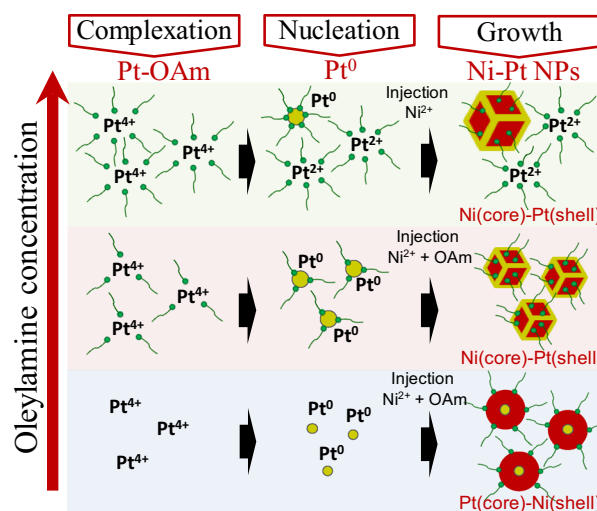
On the other hand, all the Ni–Pt NPs synthesized using a Ni:Pt precursor ratio of 95:5 and low concentration of OAm at the nucleation stage showed decomposition of methylene blue as shown in Fig. S4(e)-(h). The maximum decomposition was exhibited when Ni–Pt NPs synthesized using an OAm/Pt = 1.6 was used. When the above results were compared with the elemental mapping data, it was confirmed that the concentration of Pt on the particle surface increased with the concentration of OAm. It should be noted that the catalytic activity of Ni–Pt NPs synthesized using an OAm/Pt = 1.6 was higher than the cage structured particles synthesized using a similar amount of Pt NPs. On the other hand, the catalytic activity of the particles synthesized under higher Pt concentration that is a Ni:Pt precursor ratio of 90:10, while maintaining OAm/Pt ratio at 1.6, was almost similar or a little lesser than the low Pt concentration case (Fig. S4(i)). These results suggested that besides the segregation of Pt on the surface their thickness and their interaction with Ni atoms are also critical for higher catalytic activity. Thus, efforts should be made

Table 1 Influence of the OAm concentration in the composition, size, andstructure of synthesized Ni–Pt NPs

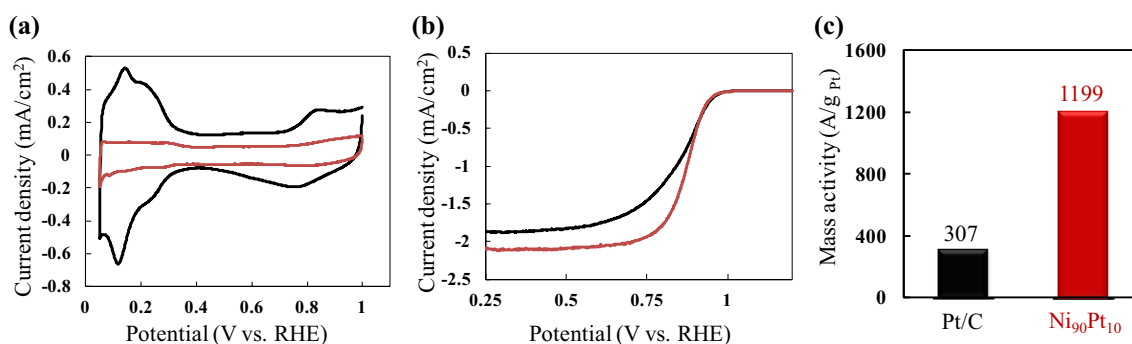| Molar ratio (OAm/Pt)	Precursor ratio (Ni:Pt)	Composition (Ni:Pt)	Crystallite size (nm)	Particle size (nm)	Structure
0	95:5	95:5	13.5 (Ni phase)	24.9	Pt core Ni shell
0.7	95:5	95:5	5.1	12.4	Alloy
1.0	95:5	95:5	5.4	13.8	
1.3	95:5	96:4	8.2	15.0	
1.6	95:5	96:4	11.0	16.2	Ni core Pt shell
1.6	90:10	91:9	7.2	14.8	

Fig. 7 **a** CV, **b** LSV (2500 rpm) curves and **c** mass activities of commercial Pt/C (black) and Ni90Pt10/C (red) catalyst

to synthesize designed Ni–Pt NPs with varying concentrations of Pt on the surface in different segregated morphologies and sizes. In addition, complete alloying should also be attempted for different sized Ni–Pt particles.

3.5 Catalytic activity of Pt and Ni–Pt NPs with 10% Pt using ORR evaluation

Based on the catalytic evaluation results, high surface area carbon supported $Ni_{90}Pt_{10}$ NPs were considered for electrocatalytic examination. The results were compared with that of commercial Pt catalyst. Figure 7(a) shows the CV measurements for Pt/C and $Ni_{90}Pt_{10}$/C samples. The ECSA evaluated for Pt/C and $Ni_{90}Pt_{10}$/C samples were 75 and 33 $m^2g^{-1}Pt$, respectively. The reason for the difference in ECSA between $Ni_{90}Pt_{10}$/C and Pt/C was due to the surface area resulting from the difference in particle size. The Pt NPs were only 3 nm in diameter in contrast to $Ni_{90}Pt_{10}$, which is about 14.8 nm [62]. However, the $Ni_{90}Pt_{10}$/C exhibited a shift in the high voltage region of the LSV curve suggesting high catalytic performance than Pt/C as shown in Fig. 7b. Furthermore, the mass activity of the above samples was estimated using the Koutecký–Levich equation based on the LSV curve obtained under different rpm for an applied voltage of 0.9 V. It should be noted that in spite of the fact that $Ni_{90}Pt_{10}$/C contained only 10% of Pt, the mass activity was four times larger than that of Pt/C and the results are shown in Fig. 7c. Thus, we strongly believe that $Ni_{90}Pt_{10}$ with Pt-enriched surface could be considered as a potential catalyst.

4 Conclusions

The technology to synthesize designed Ni–Pt NPs with different Pt distribution has been developed. The behavior of Pt-OAm complex, the key for designed-synthesis has been successfully elucidated using the in situ UV–Vis and XAS analyses. During the reaction, the –OH ligand is replaced

with $-NH_2$. The complex between Pt and OAm inhibits the reduction of Pt and results in low yield. Based on the above information, a novel synthesis scheme is proposed to synthesize Ni–Pt NPs with varying sizes and compositions. Here, the successful synthesis of Ni–Pt NPs in high yield is realized by forming the Pt nucleus under a very low concentration of OAm and introducing Ni precursor with a high concentration of OAm later. The optimal condition for the synthesis of Ni–Pt NPs with Pt on their surface is achieved when the molar ratio OAm/Pt was 1.6. As a result, high catalytic activity is achieved when the size of the particle is smallest and the Pt concentration is high. Thus, $Ni_{90}Pt_{10}$ exhibited a higher mass activity than commercial Pt in ORR The surface coverage of Pt atoms seems to have influenced the catalytic activity and further enhancement could be anticipated by improving the concentration of Pt atoms on the surface by aiming nearly alloy Ni–Pt NPs.

Compliance with ethical standards

Conflict of interest The authors declare that they have no conflict of interest.

References

1. Fratoddi I, Matassa R, Fontana L, Venditti I, Familiari G, Battocchio C, Magnano E, Nappini S, Leahu G, Belardini A, Li Voti R, Sibilia C (2017) Electronic properties of a functionalized noble metal nanoparticles covalent network. J Phys Chem C 121:18110–18119

2. Siegel J, Staszek M, Polívková M, Řezníčková A, Rimpelová S, Švorčík V (2016) Green synthesized noble metals for biological applications. Mater Today 3:608–616

3. Giner-Casares JJ, Henriksen-Lacey M, Coronado-Puchau M, Liz-Marzán LM (2016) Inorganic nanoparticles for biomedicine: where materials scientists meet medical research. Mater Today 19:19–28

4. Kwizera EA, Chaffin E, Shen X, Chen J, Zou Q, Wu Z, Gai Z, Bhana S, O'Connor R, Wang L, Adhikari H, Mishra SR, Wang Y, Huang X (2016) Size- and shape-controlled synthesis and properties of magnetic-plasmonic core–shell nanoparticles. J Phys Chem C 120:10530–10546

5. Ji X, Shao R, Elliott AM, Stafford RJ, Esparza-Coss E, Bankson JA, Liang G, Luo ZP, Park K, Markert JT, Li C (2007) Bifunctional gold nanoshells with a superparamagnetic iron oxide-silica core suitable for both MR imaging and photothermal therapy. J Phys Chem C 111:6245–6251

6. Goon Y, Lai LMH, Lim M, Munroe P, Gooding JJ, Amal R (2009) Fabrication and dispersion of gold-shell-protected magnetite nanoparticles: systematic control using polyethyleneimine. Chem Mater 21:673–681

7. Teng X, Liang X, Maksimuk S, Yang H (2006) Synthesis of porous platinum nanoparticles. Small 2:249–253

8. Cao Z, Li H, Zhan C, Zhang J, Wang W, Xu B, Lu F, Jiang Y, Xie Z, Zhenga L (2018) Monocrystalline platinum–nickel branched nanocages with enhanced catalytic performance towards the hydrogen evolution reaction. Nanoscale 10:5072–5077

9. Xia BY, Wang JN, Wang XX (2009) Synthesis and application of Pt nanocrystals with controlled crystallographic planes. J Phys Chem C 113:18115–18120

10. Rabis A, Rodriguez P, Schmidt TJ (2012) Electrocatalysis for polymer electrolyte fuel cells: recent achievements and future challenges. ACS Catal 2:864–890

11. Debe MK (2012) Electrocatalyst approaches and challenges for automotive fuel cells. Nature 486:43–51

12. Wagner FT, Lakshmanan B, Mathias MF (2010) Electrochemistry and the future of the automobile. J Phys Chem Lett 1:2204–2219

13. Stephens IEL, Bondarenko AS, Perez-Alonso FJ, Calle-Vallejo F, Bech L, Johansson TP, Jepsen AK, Frydendal R, Knudsen BP, Rossmeisl J, Stephens IC et al (2011) Tuning the activity of Pt(111) for oxygen electroreduction by subsurface alloying. J Am Chem Soc 133:5485–5491

14. Mayrhofer KJJ, Blizanac BB, Arenz M, Stamenkovic VR, Ross PN, Markovic NM (2005) The impact of geometric and surface electronic properties of Pt-Catalysts on the particle size effect in electrocatalysis. J Phys Chem B 109:14433–14440

15. Chen JG, Menning CA, Zellner MB (2008) Monolayer bimetallic surfaces: experimental and theoretical studies of trends in electronic and chemical properties. Surf Sci Rep 63:201–254

16. Watanabe M, Tsurumi K, Mizukami T, Nakamura T, Stonehart P (2017) Activity and stability of ordered and disordered co-pt alloys for phosphoric acid fuel cells. J Electrochem Soc 141:2659–2668

17. Naitabdi A, Boucly A, Rochet F, Fagiewicz R, Olivieri G, Bournel F, Benbalagh R, Sirottib F, Galleta JJ (2018) CO oxidation activity of Pt, Zn and ZnPt nanocatalysts: a comparative study by in situ near-ambient pressure X-ray photoelectron spectroscopy. Nanoscale 10:6566–6580

18. Long NV, Ohtaki M, Nogami M (2011) Structural characterization of Pt–Pd core–shell nanoparticles by Cs-corrected STEM. J Nov Carbon Res Sci 3:40–44

19. Zhang HX, Wang C, Wang JY, Zhai JJ, Cai WB (2010) Carbon-supported Pd–Pt nanoalloy with Low Pt content and superior catalysis for formic acid electro-oxidation. J Phys Chem C 114:6446–6451

20. Long NV, Asaka T, Matsubara T, Nogami M (2011) Shape-controlled synthesis of Pt-Pd core-shell nanoparticles exhibiting polyhedral morphologies by modified polyol method. Acta Mater 59:2901–2907

21. Lim B, Jiang M, Camargo PHC, Cho EC, Tao J, Lu X, Zhu Y, Xia Y (2009) Pd-Pt bimetallic nanodendrites with high activity for oxygen reduction. Science 324:1302–1305

22. Ahrenstorf K, Heller H, Kornowski A, Broekaert JAC, Weller H (2008) Nucleation and growth mechanism of Ni_xPt_{1-x} nanoparticles. Adv Funct Mater 18:3850–3856

23. Lee YW, Kim BY, Lee KH, Song WJ, Cao G, Park KW (2013) Synthesis of monodispersed Pt-Ni alloy nanodendrites and their electrochemical properties. Int J Electrochem Sci 8:2305–2312

24. Wang D, Zhao P, Li Y (2011) General preparation for Pt-based alloy nanoporous nanoparticles as potential nanocatalysts. Sci Rep 1:37

25. Cui C, Gan L, Heggen M, Rudi S, Strasser P (2013) Compositional segregation in shaped Pt alloy nanoparticles and their structural behaviour during electrocatalysis. Nat Mater 12:765–771

26. Ahmadi M, Behafarid F, Cui C, Strasser P, Cuenya BR (2011) Long-range segregation phenomena in shape-selected bimetallic nanoparticles: chemical state effects. ACS Nano 7:9195–9204

27. Cuya HJL, Fukao S, Shinoda K, Jeyadevan B (2011) Novel standing Ni–Pt alloy nanocubes. CrystEngComm 13:3364–3369

28. Fukao S (2010) Synthesis of Cubic-shaped Ni-rich Ni_xPt_{1-x} nanoparticles and evaluation of catalytic activity Graduate Thesis. The University of Shiga Prefecture, Hikone **(in Japanese)**

29. Chen C, Kang Y, Huo Z, Zhu Z, Huang W, Xin HL, Snyder JD, Li D, Herron JA, Mavrikakis M, Chi M, More KL, Li Y, Markovic NM, Somorjai GA, Yang P, Stamenkovic VR (2014) Highly crystalline multimetallic nanoframes with three-dimensional electrocatalytic surfaces. Science 343:1339–1343

30. Xu D, Liu ZP, Yang HZ, Liu QS, Zang J, Fang JY, Zou SZ, Sun K (2009) Solution-based evolution and enhanced methanol oxidation activity of monodisperse platinum-copper nanocubes. Angew Chem Int Ed 48:4217–4221

31. Mizrahi MD, Krylova G, Giovanetti LJ, Ramallo-López JM, Liu Y, Shevchenko EV, Requejo FG (2018) Unexpected compositional and structural modification of $CoPt_3$ nanoparticles by extensive surface purification. Nanoscale 10:6382–6392

32. Wu F, Lai J, Zhang L, Niu W, Lou B, Luque R, Xu G (2018) Hierarchical concave layered triangular PtCu alloy nanostructures: rational integration of dendritic nanostructures for efficient formic acid electrooxidation. Nanoscale 10:9369–9375

33. Cai Z, Kuang Y, Qi X, Wang P, Zhang Y, Zhang Z, Sun X (2015) Ultrathin branched PtFe and PtRuFe nanodendrites with enhanced electrocatalytic activity. J Mater Chem A 3:1182–1187

34. Shan A, Chen Z, Li B, Chen C, Wang R (2015) Monodispersed ultrathin NiPt hollow nanospheres with tunable diameter and composition via a green chemical synthesis. J Mater Chem A 3:1031–1036

35. Stamenkovic VR, Fowler B, Mun BS, Wang G, Ross PN, Lucas CA, Marković NM (2007) Improved oxygen reduction activity on $Pt_3Ni(111)$ via increased surface site availability. Science 315:493–497

36. Stamenkovic VR, Mun BS, Arenz M, Mayrhofer KJJ, Lucas CA, Wang G, Ross PN, Markovic NM et al (2007) Trends in electrocatalysis on extended and nanoscale Pt-bimetallic alloy surfaces. Nat Mater 6:241–247

37. Carpenter MK, Moylan TE, Kukreja RS, Atwan MH, Tessema MM (2012) Solvothermal Synthesis of platinum alloy nanoparticles for oxygen reduction electrocatalysis. J Am Chem Soc 134:8535–8542

38. Zhang J, Yang H, Fang J, Zou S (2010) Synthesis and oxygen reduction activity of shape-controlled Pt_3Ni nanopolyhedra. Nano Lett 10:638–644

39. Wu JB, Gross A, Yang H (2011) Shape and composition-controlled platinum alloy nanocrystals using carbon monoxide as reducing agent. Nano Lett 11:798–802

40. Cui C, Heggen M, Rudi S, Strasser P (2013) Compositional segregation in shaped Pt alloy nanoparticles and their structural behaviour during electrocatalysis. Nat Mater 12:765–771

41. Wang GF, Van HMA, Ross PN, Baskes MI (2005) Monte Carlo simulations of segregation in Pt–Ni catalyst nanoparticles. J Chem Phys 122:024706

42. Wu Y, Cai S, Wang D, He W, Li Y (2012) Syntheses of water-soluble octahedral, truncated octahedral, and cubic Pt–Ni nanocrystals and their structure-activity study in model hydrogenation reactions. J Am Chem Soc 134:8975–8981

43. Ding J, Bu L, Guo S, Zhao Z, Zhu E, Huang Y, Huang X (2016) Morphology and phase controlled construction of Pt–Ni nanostructures for efficient electrocatalysis. Nano Lett 16:2762–2767

44. Yang H, Vogel W, Lamy C, Alonso-Vante N (2004) Structure and electrocatalytic activity of carbon-supported Pt–Ni alloy nanoparticles toward the oxygen reduction reaction. J Phys Chem B 108:11024–11034

45. Zhang S, Hao Y, Su D, Doan-Nguyen VVT, Wu Y, Li J, Sun S, Murray CB (2014) Monodisperse core/shell Ni/FePt nanoparticles and their conversion to Ni/Pt to catalyze oxygen reduction. J Am Chem Soc 136:15921–15924

46. Nagao A, Higashimine K, Cuya HJL, Iwamoto K, Matsumoto T, Inoue Y, Maenosono S, Miyamura H, Jeyadevan B (2015) Formation of Pt decorated Ni–Pt nanocubes through low temperature atomic diffusion—time-resolved elemental analysis of nanoparticle formation. Nanoscale 7:9927–9934

47. Mourdikoudis S, Liz-Marzan LM (2013) Oleylamine in nanoparticle synthesis. Chem Mater 25:1465–1476

48. CS Chem3D Ver.7.0, CambridgeSoft Corporation (Cambridge Scientific Computing, Inc.)

49. Gaussian 09, Revision E.01, Frisch MJ, Trucks GW, Schlegel HB, Scuseria GE, Robb MA, Cheeseman JR, Scalmani G, Barone V, et al. (2013) Gaussian, Inc., Wallingford CT

50. Dunning JTH, Hay PJ (1977) Anharmonic spectroscopic investigation of tellurophene and its perdeuterated isotopomer: application of second-order perturbation theory. J Quant Chem 3:1–28

51. Hay PJ, Wadt WR (1985) Ab initio effective core potentials for molecular calculations. Potentials for the transition metal atoms Sc to Hg. J Chem Phys 82:270–283

52. Wadt WR, Hay PJ (1985) Ab initio effective core potentials for molecular calculations. Potentials for main group elements Na to Bi. J Chem Phys 82:284–298

53. Hay PJ, Wadt WR (1985) Ab initio effective core potentials for molecular calculations. Potentials for K to Au including the outermost core orbitals. J Chem Phys 82:299–310

54. Ishijima M, Cuya HJL, Yokoyama S, Shinoda K, Uchikoshi M, Miyamura H, Jeyadevan B (2018) In situ spectroscopic studies of the one-pot synthesis of composition-controlled Cu–Ni nanowires with enhanced catalytic activity. New J Chem 42:13044–13053

55. Herricks T, Chen J, Polyol Xia Y (2004) Synthesis of platinum nanoparticles: control of morphology with sodium nitrate. Nano Lett 4:2367–2371

56. Chen J, Herricks T, Geissler M, Xia YJ (2004) Single-crystal nanowires of platinum can be synthesized by controlling the reaction rate of a polyol process. Am Chem Soc 126:10854–10855

57. Mizukoshi Y, Takagi E, Okuno H, Oshima R, Maeda Y, Nagata Y (2001) Preparation of platinum nanoparticles by sonochemical reduction of the Pt(IV) ions: role of surfactants. Ultrason Sonochem 8:1–6

58. Bel'skayaa OB, Karymovaa RK, Kochubeib DI, Duplyakina VK (2008) Genesis of the active-component precursor in the synthesis of Pt/Al$_2$O$_3$ catalysts: I. Transformation of the [PtCl6]$^{2-}$ complex in the interaction between chloroplatinic acid and the γ-Al$_2$O$_3$ surface. Kinet Catal 49:720–728

59. Niu Z, Becknell N, Yu Y, Kim D, Chen C, Kornienko N, Somorjai GA, Yang P (2016) Anisotropic phase segregation and migration of Pt in nanocrystals en route to nanoframe catalysts. Nat Mater 15:1188–1194

60. LaMer VK, Dinegar RH (1950) Theory, production and mechanism of formation of monodispersed hydrosols. J Am Chem Soc 72:4847–4854

61. Guo H, Chen Y, Ping H, Wang L, Peng DL (2012) One-pot synthesis of hexagonal and triangular nickel–copper alloy nanoplates and their magnetic and catalytic properties. J Mater Chem 22:8336–8344

62. Li B, Wang J, Gao X, Qin C, Yang D, Lv H, Xiao Q, Zhang C (2018) High performance octahedral PtNi/C catalysts investigated from rotating disk electrode to membrane electrode assembly. Nano Res. https://doi.org/10.1007/s12274-018-2211-9